An algorithm for Structural Health Monitoring by Digital Image Correlation: Proof of concept and case study

Jordan Curt, Matteo Capaldo, François Hild, Stéphane Roux

An algorithm for Structural Health Monitoring by Digital Image Correlation: Proof of concept and case study

Jordan Curt,[1,2] Matteo Capaldo,[1] François Hild[2] and Stéphane Roux[2]

[1] EDF Research & Development, 91120 Palaiseau, France
[2] Université Paris-Saclay, ENS Paris-Saclay, CNRS, LMT - Laboratoire de Mécanique et Technologie, 91190 Gif-sur-Yvette, France

Abstract

In the field of structural health monitoring, the use of Digital Image Correlation (DIC) on relevant surfaces offers remarkable advantages. Such a method is presented herein. The statistically stationary nature of usual loads makes it possible to determine, by training with DIC, a reduced kinematic basis (composed of "modes") and a statistical amplitude distribution for each mode. Further, a specific DIC technique is proposed to deal with such particular kinematics by introducing an extractor per mode that operates on images after a filtering step. This per-mode DIC measurement is reduced to a simple scalar product between the image and the corresponding extractor, which allows for very fast and non-iterative processing. As an illustration, this methodology is deployed on a test case of fatigue crack propagation.

1 Introduction

Over the course of its life, a structure is often subjected to repetitive loading that may lead to the occurrence of damage [1]. The latter can take the form of local yielding areas, open cracking or diffuse microcracking. Being able to detect these defects is essential to ensure structural integrity over time. However, when the considered structure has a very large surface area, such as a bridge, it is complicated to monitor it exhaustively. To reduce costs, methods for continuous monitoring of structures and automatic detection of defects have been developed over time. These techniques are often based on continuous recording of data from sensors that are assumed to reflect the health state of a structure as a whole. A drift of the measured quantities is expected in the event of a defect appearing within a structure [2].

The main type of sensor used for structural health monitoring (SHM) applications is the accelerometer, which allows for a modal characterization of a structure (*i*.e., eigenfrequency

variation over time [3]). Other frequently used sensors include strain gauges and optical fibers, which give access to local strains [4, 5]. They detect an increase in the measured strains over time, which then allows for damage detection. The main disadvantage of these techniques is that they extrapolate local data to obtain an estimate of the overall health state. A lack of sensitivity is to be feared for defects that remain latent for macroscopic characteristics of the structure until their growth becomes catastrophic. To alleviate that risk, turning to optical methods that allow for exhaustive views has been proposed [6–8]. The objective is then to automatically detect the presence of defects on the structure surfaces. Such a principle is usually limited to thin structures.

At first glance, visible damage and more particularly cracks implies a local intensity variation on the structure surface. Algorithms exist to detect the contours of objects on images at pixel resolutions [9, 10], and sub-pixel scales [11–13]. These algorithms have inspired the development of methods for automatic recognition of surface defects on concrete samples [14, 15] or on bridges [16] for instance. They can be coupled with the use of specific robots equipped with cameras connected to an image processing device for fast and yet exhaustive inspections [17].

The disadvantage of these techniques is that they lack robustness because they are based on a gradient threshold. Its choice will greatly influence the type of detected discontinuity. To make these approaches more robust, couplings with deep-learning algorithms have been proposed. The algorithm is trained on a large number of images to recognize a particular defect [18–20]. The automatic detection then becomes more "customized" to a specific structure and/or material, but these techniques do not *ensure* damage detection. In addition, their training requires a large set of data to be available. To increase their reliability, it has been suggested to train neural networks on several types of materials (assuming that they all share comparable defects) [21].

Despite the use of deep-learning algorithms, the important drawback that remains with methods based on contour detection is that damage must be clearly visible on the surface with apparent crack opening. If it is faintly visible or underlying, it may not be detected and such risk is not acceptable for SHM purposes. When damage is present, be it apparent or not, it will necessarily have a local signature on the way the surface will deform when subjected to in-service loading. Digital Image Correlation (DIC) is a well known technique in the experimental field to measure surface displacement fields between reference and deformed states [22–24]. Such a tool has been largely used to study damage phenomena [25–28]. More precisely, methods using DIC have been developed to automatically detect damage within a structure, especially cracks. The simplest methods seek to detect large strains due to crack-induced displacement jumps. They have been extended to several fields such as masonry [29], composite materials [30] or renewable energies [31]. However, such methods may exhibit poor robustness because, as for contour detection, threshold levels are difficult to estimate, especially if the structure is subjected to multiaxial loadings.

The precise quantification of cracks by DIC in mechanical tests has been subject of numerous

developments in order to determine the precise position of the crack tip [32, 33], to calculate stress intensity factors in post-processing steps [34, 35] and via integrated DIC [32, 36], or to study the entire crack path [37, 38]. Many of these techniques were not intended to automatically detect the presence of cracks on a surface, as they require non-obvious initial calibration. However, they could be diverted to automate the detection. For example, in Ref. [39], the displacement was initially sought on the basis of simple kinematic bases (*e*.g., accounting for rigid body motions and uniform strains). Damaged areas then are synonymous for higher correlation residuals, which are obtained from image differences after registration. Based on the knowledge of the displacement field around a crack, it was then possible to iteratively adjust the position, orientation and length of several cracks within the area of interest. For this method, it is therefore necessary that the cracks be open, and that the deformations undergone by the structure be not too complex.

In order to gain robustness, methods have emerged based on the knowledge of the displacement field when the structure is sound. If, during the experiment or over time, a defect induces a variation in terms of displacement fields with respect to the *healthy* specimen, it will be detected using specific indicators. In Ref. [40], a concrete sample was subjected to 4-point bending under increasing load over time. At each step, the displacement field measured via DIC was decomposed using wavelets. The comparison between the first load level and the following ones allows an indicator of energy drift to be established over all the decomposition stages. The occurrence of damage induced a variation in the decomposition form, which resulted in an increase in the error indicator. With such a method, it is difficult to evaluate the sensitivity to the defect, especially since the example dealt with concrete that easily damages under bending. Moreover, the method seems complicated to calibrate because of the many possible variations for the wavelet decomposition.

In Ref. [41], a method for estimating the residual life of a drilled composite specimen in a tensile fatigue test was presented. Strains of the material were estimated by DIC at several instances of time during the test, always at maximum load level. Through multiple tests, a life estimation model was calibrated using a learning algorithm. Over time, damage indicators were calculated to predict the remaining service life. This type of method using DIC is robust to identify structural damage when the test conditions are well known, and when several samples are available to calibrate the model. Its use in real conditions seems delicate given that model calibration involves complex algorithms.

The objective of this work is to introduce a new autonomous structural health monitoring method based on DIC for structures that undergo statistically stationary loading during their lifetime, which is the case of many industrial structures. Only the algorithm and a proof of concept are presented. Its practical implementation is beyond the scope of the present paper. The idea consists in using very simple model order reduction methods to describe the displacement field viewed by a single or multiple camera(s). Such techniques have already been conducted using DIC data. First, in Ref. [42] from 350 random time shots of a vibrating plate,

8 main modes of the structure were found by principal component analysis. These modes were orthogonalized with respect to the mass matrix of the finite element model in order to coincide with actual vibration modes. The comparison between these modes and the numerical predictions was conclusive. In Ref. [43], the 3D displacement fields measured during a thermomechanical test, which were initially very noisy, were decomposed on a reduced modal basis in order to reduce unphysical temporal fluctuations. In the case of that test, a unique mode was used to describe almost all the kinematics of the experiment. The idea of restricting the kinematic space has also been pursued for modal analysis [44]. A unique sinusoidal temporal mode, which was related to the vibration mode, was used.

The proposed method is decomposed into two steps. First, during the learning stage, a kinematic modal basis is determined from a set of pictures taken on the undamaged structure with a variety of (natural) loadings. In the second stage, namely that of health monitoring, new pictures are acquired, and the measured displacement fields are projected onto the initial modal basis. This second step consists, in fact, in performing a large number of times "integrated DIC." It utilizes finite element shape functions extracted from a model or inspired by physics. If a defect initiates, differences appear in global error indicators that will highlight it either from displacements or correlation residuals. In order to simplify image processing of this second step, a new "one-step DIC" strategy is introduced, which reduces DIC processing to a mere scalar product of the difference between current and reference images with one extractor field per mode. This DIC scheme is performed on filtered images, where the filter is tailored to the observed displacement field. The method is illustrated on a fatigue crack propagation experiment.

2 Damage detection via DIC

2.1 DIC principle

Digital Image Correlation (DIC) is a displacement field measurement technique that allows the image of a surface in its reference state to be registered with that of the deformed configuration. These two images are respectively described by matrices f and g representing the gray levels associated with the pixel at position $\boldsymbol{x}$. By noting $\boldsymbol{u}$ the displacement field between the two images, the following equation

$$f(\boldsymbol{x}) = g(\boldsymbol{x} + \boldsymbol{u}(\boldsymbol{x})) \tag{1}$$

accounts for gray level conservation. The objective is to find the displacement field that minimizes the cost function defined as the sum of quadratic gray level differences. It is convenient to discretize the displacement field via, say, finite element shape functions $\boldsymbol{n}_i(\boldsymbol{x})$ with unknown nodal displacements a_i

$$\boldsymbol{u}(\boldsymbol{x}) = \sum_i a_i \boldsymbol{n}_i(\boldsymbol{x}) \tag{2}$$

Based on the minimization of the cost function over the considered region of interest (ROI),

displacements are determined via modified Gauss-Newton scheme where incremental corrections to the nodal displacements are obtained from the linear problem

$$[\boldsymbol{M}]\{\delta\boldsymbol{a}\} = \{\boldsymbol{b}\} \tag{3}$$

with

$$M_{ij} = \sum_{\boldsymbol{x}} (\boldsymbol{n}_i(\boldsymbol{x}) \cdot \boldsymbol{\nabla} f(\boldsymbol{x}))(\boldsymbol{n}_j(\boldsymbol{x}) \cdot \boldsymbol{\nabla} f(\boldsymbol{x})) \tag{4}$$

and

$$b_i = \sum_{\boldsymbol{x}} (\boldsymbol{n}_i(\boldsymbol{x}) \cdot \boldsymbol{\nabla} f(\boldsymbol{x}))(f(\boldsymbol{x}) - \tilde{g}_{\{\boldsymbol{a}\}}(\boldsymbol{x})) \tag{5}$$

where $[\boldsymbol{M}]$ is the DIC matrix, and $\{\boldsymbol{b}\}$ the second-member. In the above equation, $\tilde{g}_{\{\boldsymbol{a}\}}$ is the deformed image g corrected by the current determination $\{\boldsymbol{a}\}$ of the nodal displacements

$$\tilde{g}_{\{\boldsymbol{a}\}}(\boldsymbol{x}) = g\left(\boldsymbol{x} + \sum_i a_i \boldsymbol{n}_i(\boldsymbol{x})\right) \tag{6}$$

When convergence is reached, the difference $\eta(\boldsymbol{x}) = \tilde{g}_{\{\boldsymbol{a}\}}(\boldsymbol{x}) - f(\boldsymbol{x})$ is called correlation residual.

In some cases, gray level conservation may be violated due to small illumination variations of the experimental scene. The optical flow is then enriched thanks to gray level corrections.

2.2 Gray level correction

A commonly adopted way to account for gray level corrections is provided by affine transformation of the gray level scale [23, 45–50]

$$c(\boldsymbol{x}) + (1 + d(\boldsymbol{x}))f(\boldsymbol{x}) = g(\boldsymbol{x} + \boldsymbol{u}(\boldsymbol{x})) \tag{7}$$

where c and d are spatially varying fields. As the displacement field, they are discretized over the whole ROI thanks to scalar shape functions $m_i(\boldsymbol{x})$

$$c(\boldsymbol{x}) = \sum_i c_i m_i(\boldsymbol{x}) \tag{8}$$

$$d(\boldsymbol{x}) = \sum_i d_i m_i(\boldsymbol{x}) \tag{9}$$

The determination of the nodal amplitudes c_i and d_i relies on linear problem solving. They can be calculated either in the same loop as the displacements [23], or alternatively after it if their contribution is small [51].

2.3 Model order reduction

2.3.1 Principle

Model order reduction techniques are used to lower the number of degrees of freedom grouping a set of fields. The Principal Component Analysis (PCA) [52], which is similar to the Proper Orthogonal Decomposition (POD) [53], is used to bring out the most important information in data sets. Let us consider a problem with n spatial degrees of freedom whose solutions are available at n_t time steps. The matrix $[\mathbf{A}]$ is the concatenation of solutions in time, then its dimension is $n \times n_t$. PCA gives a factorization of rectangular matrix $[\mathbf{A}]$

$$[\mathbf{A}] = [\mathbf{V}][\mathbf{\Sigma}][\mathbf{U}]^\top \tag{10}$$

where $[\mathbf{V}]$ is the $n \times n$ matrix of the orthonormal spatial modes that form a canonical basis $\boldsymbol{\psi_i}(\boldsymbol{x})$, $[\mathbf{\Sigma}]$ the $n \times n_t$ diagonal matrix where the non-zero terms are considered as the singular values of the matrix, and $[\mathbf{U}]$ the $n_t \times n_t$ matrix of orthonormal temporal modes denoted by $\phi_i(t)$ in the sequel. From this decomposition, the singular values account for the importance of the modes in the decomposition. The higher the value, the more important the mode for the global field description. Such a method is applied to a set of displacements field measured via DIC

$$\boldsymbol{u}(\boldsymbol{x}, t) = \sum_i^n \alpha_i \boldsymbol{\phi}_i(t) \boldsymbol{\psi}_i(\boldsymbol{x}) \tag{11}$$

with α_i the i-th singular value, $\boldsymbol{\phi}_i$ the i-th temporal mode and $\boldsymbol{\psi}_i$ the corresponding i-th spatial mode, where both $\boldsymbol{\phi}_i$ and ψ_j are normalized.

This set of modes can be truncated and it results in efficient data reduction. The selection of the appropriate number n_a of modes is based on α_i values. If they reach levels close to measurement uncertainty, the mode is no longer relevant to adequately describe the displacement fields. The approximate displacement field $\boldsymbol{u_a}$ is then defined as

$$\boldsymbol{u_a}(\boldsymbol{x}, t) = \sum_i^{n_a} \alpha_i \boldsymbol{\phi}_i(t) \boldsymbol{\psi}_i(\boldsymbol{x}) \tag{12}$$

2.3.2 Uncertainty consideration

It is noteworthy that, implicitly, the metric used for model reduction is the (Euclidean) L_2 norm. A relevant metric in the case of model reduction is that related to measurement uncertainty [54]. For DIC, this information is contained in the DIC matrix $[\boldsymbol{M}]$. Its consideration in model order reduction is completed by weighting the mesh nodes displacement values by the square root of the DIC matrix. PCA then yields

$$[\boldsymbol{M}]^{\frac{1}{2}}[\boldsymbol{u}] = [\mathbf{\Psi}^*][\mathbf{\Sigma}^*[\mathbf{\Phi}]^{*\top} \tag{13}$$

where $[\boldsymbol{\Psi}^*]$ is the matrix related to the spatial modes, $[\boldsymbol{\Sigma}^*]$ the diagonal matrix, $[\boldsymbol{u}]$ the matrix gathering in columns the measured spatiotemporal nodal displacements, and $[\boldsymbol{\Phi}^*]$ the matrix associated with the temporal modes. It is worth noting that the columns of $[\boldsymbol{\Psi}^*]$ are no longer displacements and admittedly their interpretation is not straightforward. However, they can be transformed into displacement modes $\boldsymbol{\psi}_i$

$$\{\boldsymbol{\Psi}_i\} = [\boldsymbol{M}]^{-\frac{1}{2}}\{\boldsymbol{\Psi}_i^*\} \tag{14}$$

with $\{\boldsymbol{\Psi}_i^*\}$ the i-th column of $[\boldsymbol{\Psi}^*]$. In the following, examples of both matrices $[\boldsymbol{\Psi}_i]$ and $[\boldsymbol{\Psi}_i^*]$ will be shown and commented. The PCA technique is performed based on a truncation of the diagonal matrix $[\boldsymbol{\Sigma}^*]$, thereby leading to a consistent model reduction based on the statistical properties of random uncertainties affecting the processed data (*i*.e., images).

2.4 Damage detection

The modal displacement basis is set up from a large number of images when the structure is subjected to statistically repeated loading. This step is the learning stage of the proposed method, and the structure is assumed to be sound (*i*.e., undamaged). These images can be pre-processed by "subtracting" rigid body translations by FFT-DIC for instance [55]. To account for illumination variations that may occur, brightness and contrast corrections are applied after seeking for the displacement, as these variations remain small. From this data gathering, the statistics about the modal amplitudes and residuals are deduced. A drift in those levels is synonymous with damage occurrence.

During the monitoring phase, new pictures are acquired multiple times and displacements are measured. These fields are projected onto the *sound* (*i*.e., undamaged) modal basis, and a projection gap is deduced. This error is calculated as the difference between the displacement initially measured by DIC and that resulting from its projection onto the considered modal basis. For damaged states, the error will increase because damage was not integrated into the modal basis. Thus, based on displacement and also DIC projection residuals, error indicators can be set to detect damage onset.

3 Case study: Fatigue crack propagation

The main features of the proposed method are illustrated in this section, which is based upon an experimental case study dealing with crack propagation.

3.1 Mechanical test

The selected experiment consisted in testing a Center Cracked Tension (CCT) specimen made of 2024 aluminium alloy. This material is classically used in aeronautics and aerospace industries. The sample size was $150 \times 50 \times 2$ mm with an 8 mm pre-notch machined via EDM from a 3 mm in diameter hole. One side of the sample was speckled with black and white paints for DIC purposes. The same specimen geometry was used in Ref. [56], and it was shown that the

temperature variations close to the crack tip remained very small during the whole test (*i*.e., less than 1 K). Such small fluctuations will not induce any alterations of the speckle pattern. The setup is shown in Figure 1.

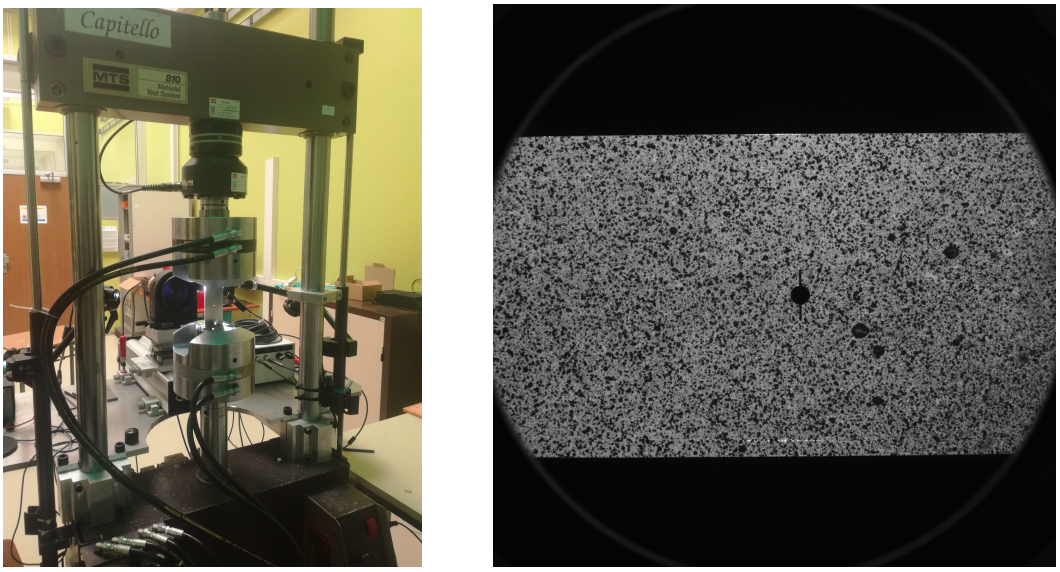

(a) (b)

Figure 1: (a) Experimental setup. (b) Specimen surface monitored by the camera

The hardware parameters of the optical setup are reported in Table 1.

Table 1: DIC hardware parameters

Camera	Allied Vision Manta G-145B
Definition	2048×2048 px
Gray Levels amplitude	16 bits
Telecentric lens	Edmund Optics $\times 0.125$
Field of view	100×100 mm^2
Image scale	50 µm/px
Stand-off distance	25 cm
Image acquisition rate	1 fps
Patterning technique	sprayed paints
Pattern size	7 px

First, the specimen was subjected to cyclic loading at 10 Hz with a tensile force of 8 kN for 7,500 cycles in order to initiate two cracks. Then the specimen was sinusoidally loaded at a frequency of 0.1 Hz with strains up to 5×10^{-4}, which corresponded to 3 kN approximately. 150 images were acquired twice. The frequency of image acquisition was 1 Hz. Thus 10 pictures per period of loading were available. In the following, the initial step will refer to

these first 150 images. It corresponds to the *learning stage*, and the modal basis is set up at this step. In this stage, the specimen is in its reference (*i*.e., undamaged) state. The second set of 150 images will be referred to as step 1. It is part of the *monitoring* stage, where the mechanical condition of the specimen is assessed over time. It will serve as reference to compare to the results obtained at the initial step, because both sets of pictures were acquired for the same damage state. Then, series of 10,000 cycles at a maximum force of 7 kN were conducted at a frequency of 10 Hz and the crack continued to propagate. Between each propagation phase, 150 images were acquired under the same loading condition as for the initial step. 3 new sets of images are available. They are referred to steps 2 to 4. The flowchart shown in Figure 2 summarises the whole experiment and the different stages. Error indicators are introduced to show that the specimen was damaged over time, using the results obtained during the *learning* stage as reference.

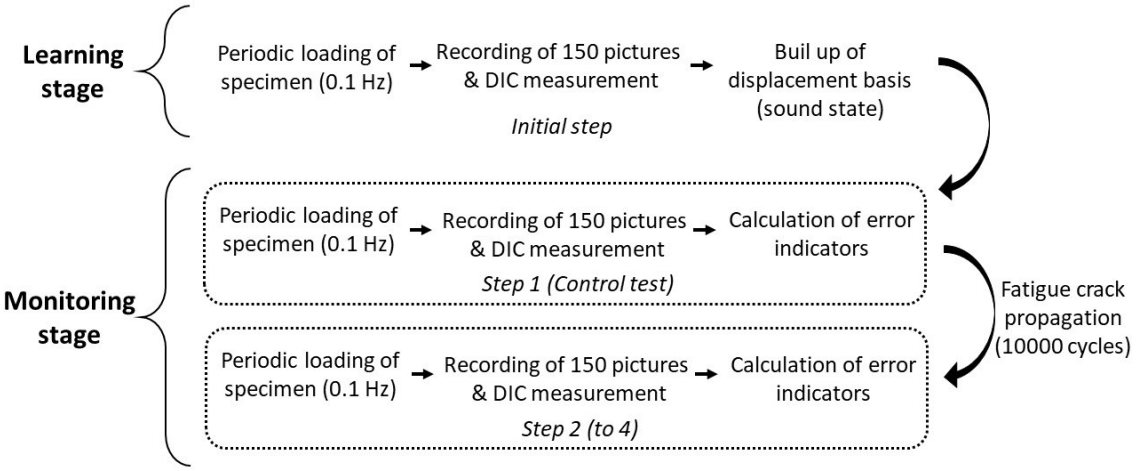

Figure 2: Flowchart summarising the whole damage detection analysis

Figure 3 shows the mesh used for this work. It is made of 3-noded triangular (T3) elements. On the right side of the ROI, a (red) box is selected to pre-calculate the rigid body translations of the specimen, thanks to FFT-DIC. The displacements obtained in both directions were stored and removed from the total displacement fields for PCA purposes.

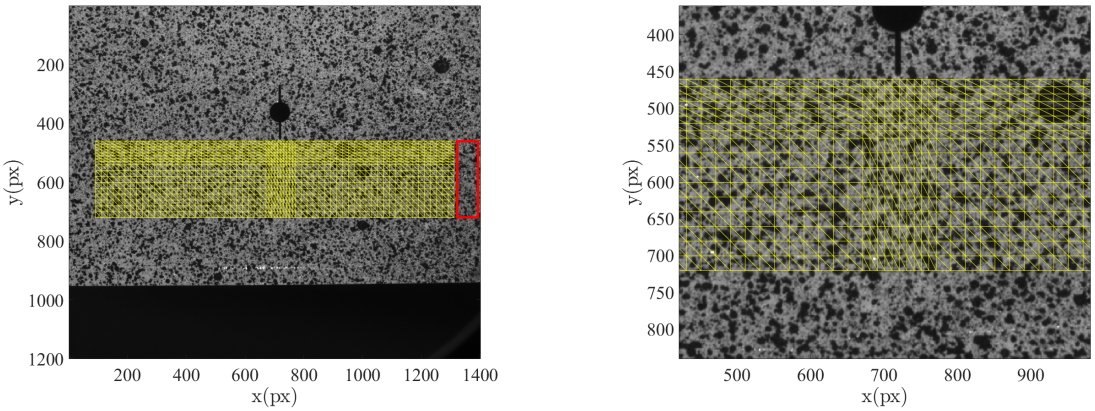

(a) (b)

Figure 3: (a) Mesh used in T3-DIC analyses. The red rectangle is the region used to pre-calculate the rigid body translations. (b) Zoom of the mesh showing the refinement close to the crack tip

The DIC analysis parameters are gathered in Table 2.

Table 2: DIC analysis parameters

DIC software	Correli 3.0 [57]
Image filtering	none
Element length	10/20 px
Shape functions	linear (T3)
Mesh	see Figure 3
Matching criterion	see text
Interpolant	cubic
Displacement noise-floor	0.024 px

3.2 Damage detection by DIC

This subsection first presents the results obtained with model order reduction techniques applied to DIC data from the *learning* stage. Then, the results on defect identification based on several error indicators are illustrated.

3.2.1 Model order reduction

As explained in Section 2.3, the mode relevance is related to its singular value. The set of singular values is plotted in Figure 4(a) for the analyzed sequence. The singular value associated with the first mode is one order of magnitude higher than the others. This observation means that it contains most of the kinematic information. The loading being unidirectional, the first

mode is associated with tension. It will be confirmed in the sequel by displaying the spatial modes.

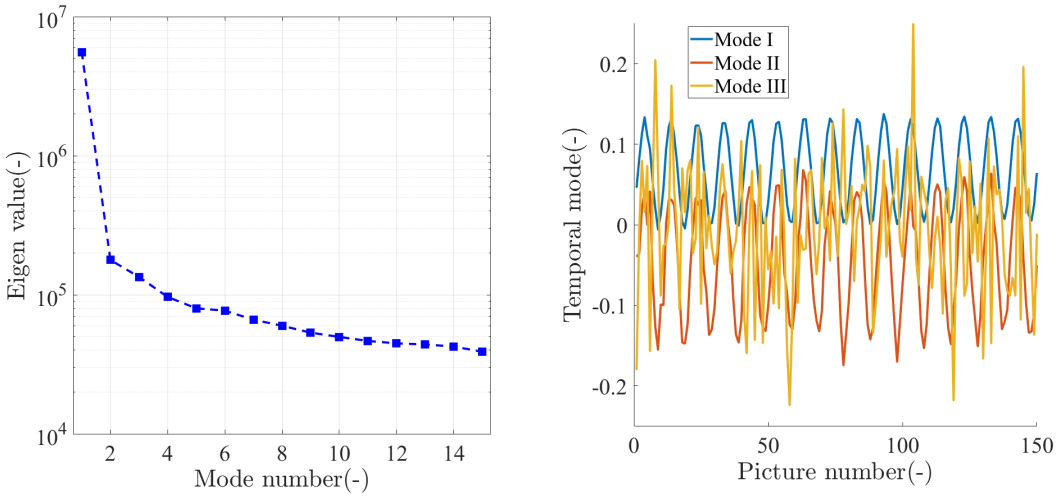

(a) (b)

Figure 4: (a) Eigen values associated with the first 15 modes. (b) Temporal modes $\phi_i(t)$

The eigenvalues related to the other modes stabilize from the fourth mode on. Thus, it is concluded that three modes are sufficient to describe the whole kinematics. The first three spatial modes are displayed in Figures 5, 6, and 7 respectively. As earlier mentioned, the direct $\mathbf{\Psi}_i^*$ modes are difficult to "read" because of the $[\boldsymbol{M}]^{\frac{1}{2}}$ weighting. However, their translations into displacement modes $\mathbf{\Psi}_i$ have a more intuitive meaning. This is illustrated for the first mode, where both raw and corresponding displacement modes are displayed in Figure 5. The raw modes are more difficult to “read” to due to the $[\boldsymbol{M}]^{\frac{1}{2}}$ weighting. As expected, the first temporal mode $\phi_i(t)$ is sinusoidal (Figure 4(b)), and its spatial representation is relative to uniaxial tension the sample was subjected to. The second temporal mode is also sinusoidal. The third temporal mode is more difficult to interpret as it is to be orthogonal to both previous temporal modes (*i*.e., orthogonal to an affine function of sine loading).

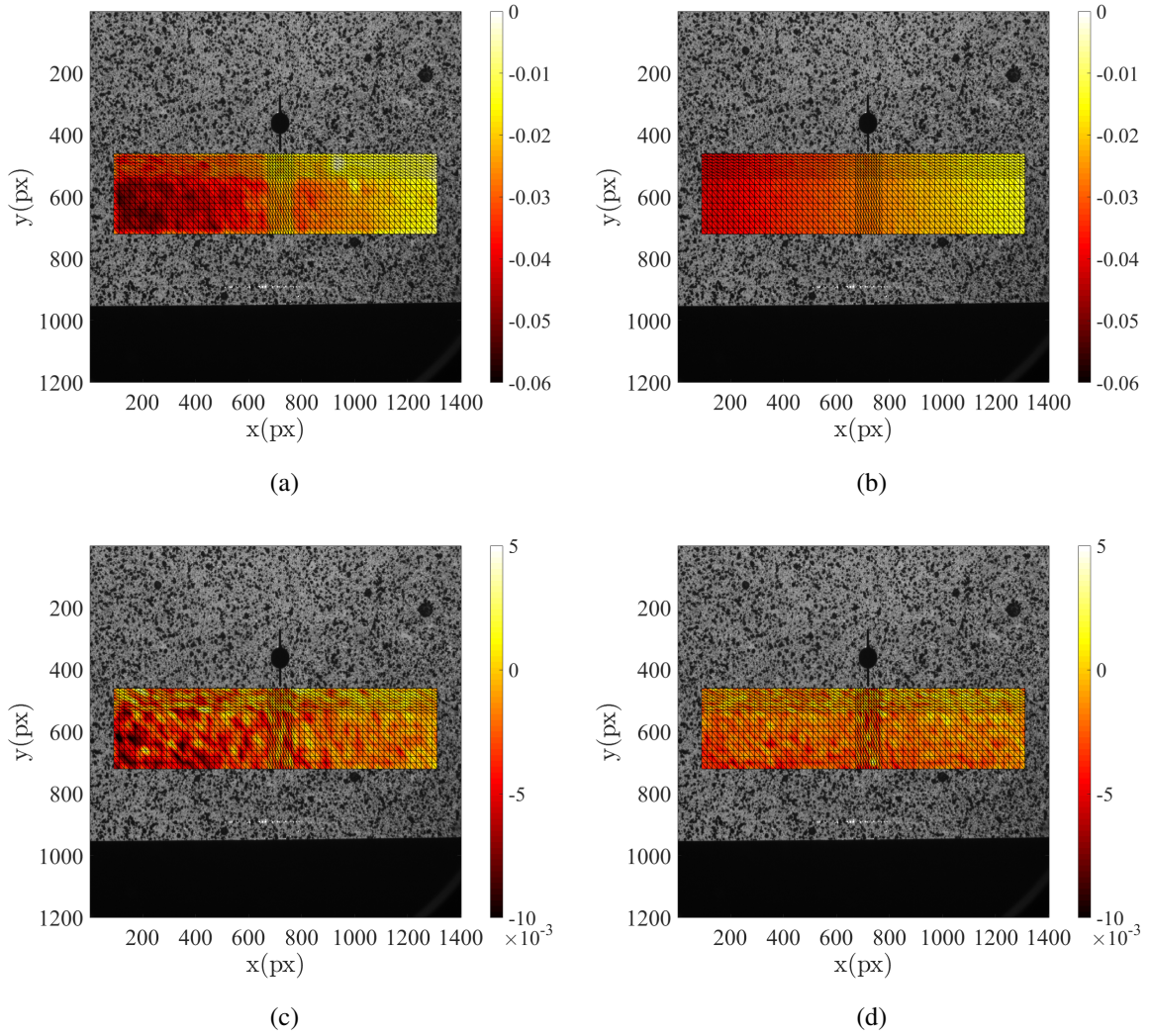

Figure 5: (a,c) First spatial mode $\mathbf{\Psi}_1^*$ respectively along x and y directions. (b,d) Corresponding displacement modes $\mathbf{\Psi}_1$

Only the second and third associated displacement modes are displayed. In contrast to the first displacement mode, the second mode is more difficult to interpret. Presumably, low eigenvectors of the DIC Hessian are present and give rise to high frequency "noise", but one notes that at long wavelengths a vertical motion in the center of the ROI is observed. The third mode contains additional rotation.

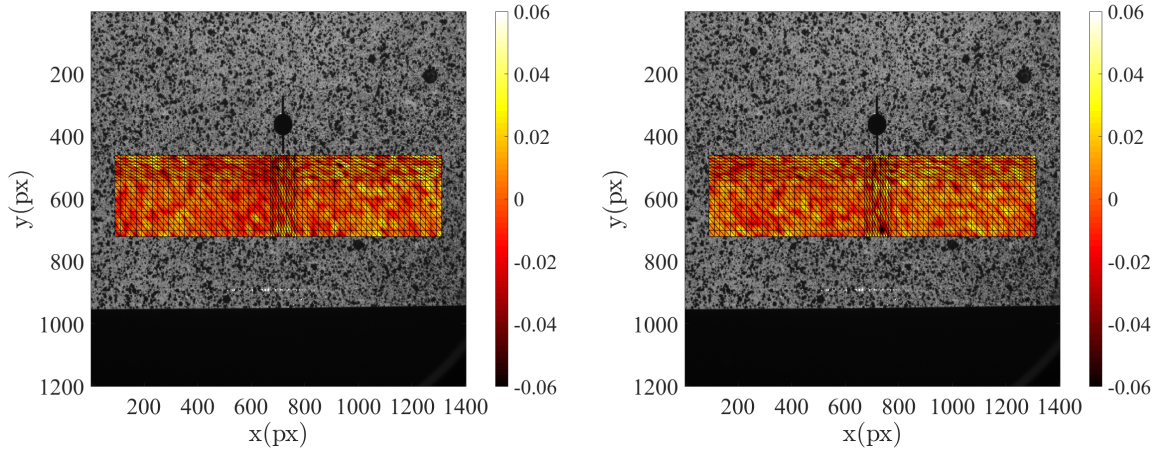

(a) (b)

Figure 6: Second spatial mode $\mathbf{\Psi}_2$ along x (a) and y (b) directions

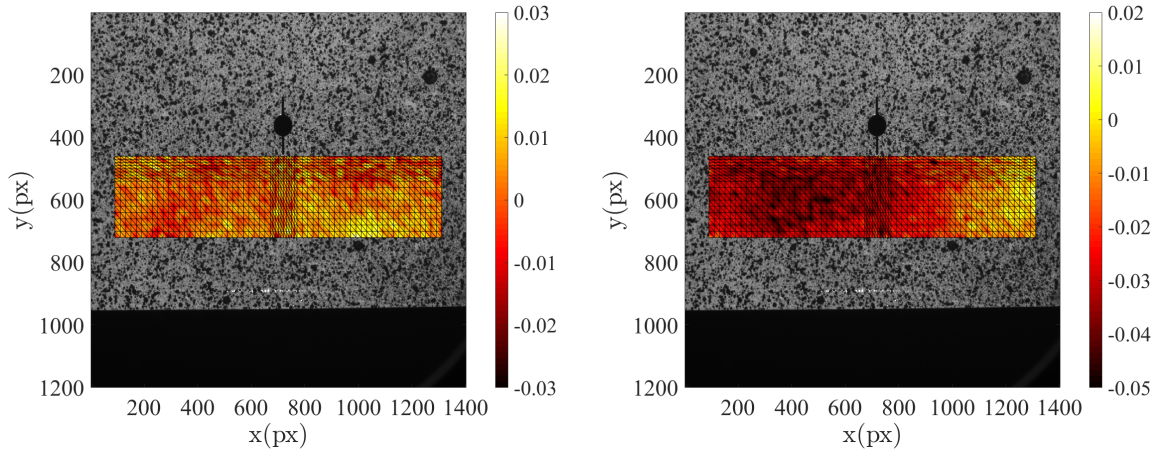

(a) (b)

Figure 7: Third spatial mode $\mathbf{\Psi}_3$ along x (a) and y (b) directions

3.2.2 Error indicators related to displacements

In order to automatically detect the presence of damage, error indicators are introduced. The measured displacement field is projected onto the modal basis determined during the learning phase. Displacement error vectors are obtained by subtracting the projected displacement fields to those initially measured by DIC at mesh nodes. From these error vectors, indicators are constructed, namely, the standard deviation and the maximum level. The indicators are plotted for the initial step and steps 1 to 4 in Figure 8. It was found that 3 modes were sufficient to describe the whole kinematics. However, the influence of the number of modes on the error levels is also studied hereafter. The indicators are plotted for 3 and 6 projection modes. For each step, the mean values of the error indicators are reported.

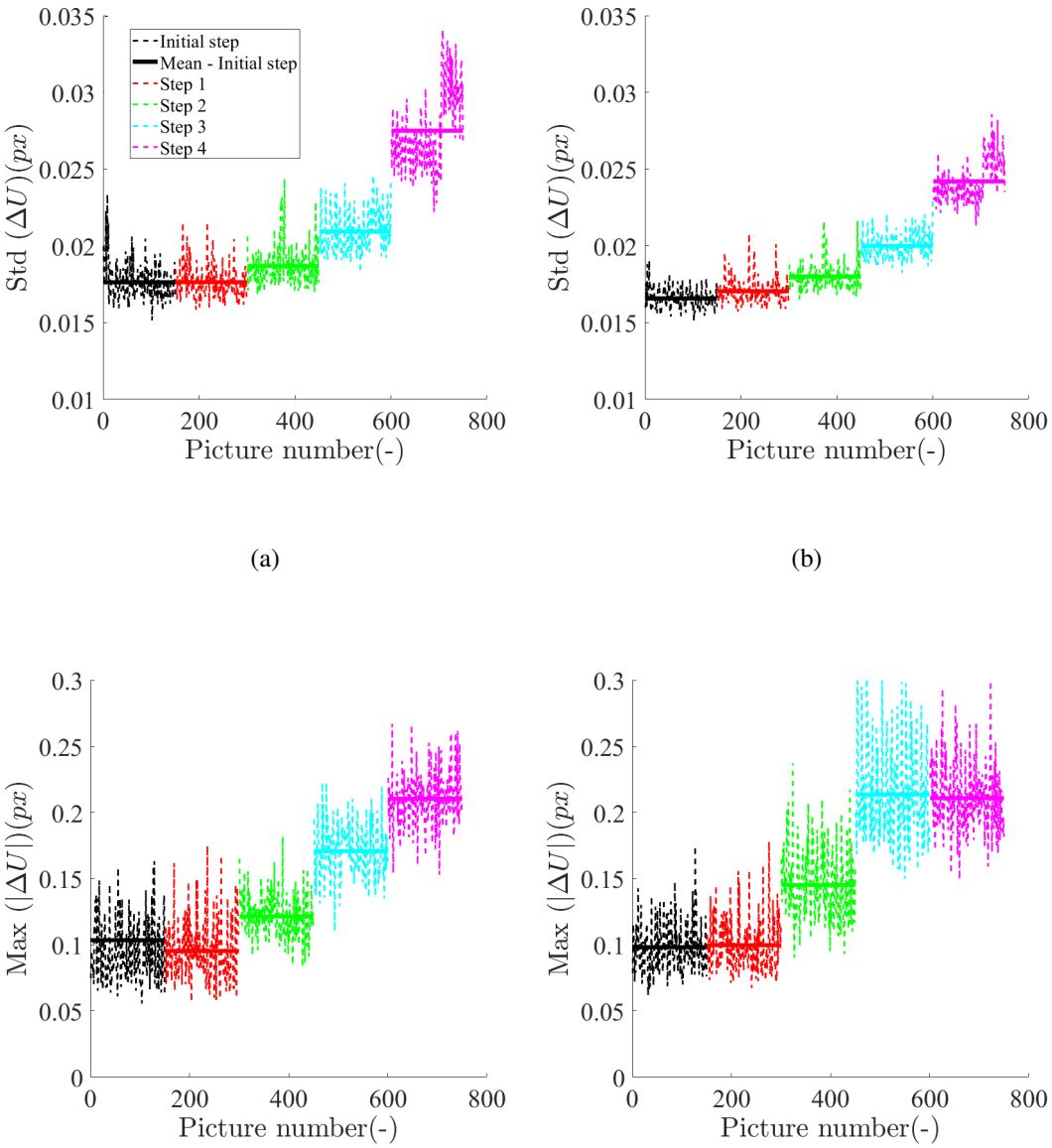

Figure 8: Projection displacement error indicators for all five steps. (a,b) Standard deviation for 3 and 6 modes respectively. (c,d) Corresponding maximum levels

First, the more the specimen is damaged (*i*.e., the crack has propagated), the higher the mean values of the error indicators. The latter ones fluctuated significantly, which stresses the importance of considering mean values over a certain period of time. This observation is even more relevant when the loading is random. The comparison of the results obtained with 3 and 6 modes suggests that the average value and the fluctuation decrease with basis enrichment for the standard deviation. For the maximum error, this trend is less obvious. Thus, a good way to evaluate indicator drift is to normalize the difference between the mean values over the initial

step and the other steps by the fluctuations (*i*.e., the standard deviation) of the initial step, as shown in Figure 9. The higher the number of modes, the more discriminating the presence of a crack for the normalized standard error. It is not the case for the normalized maximum error.

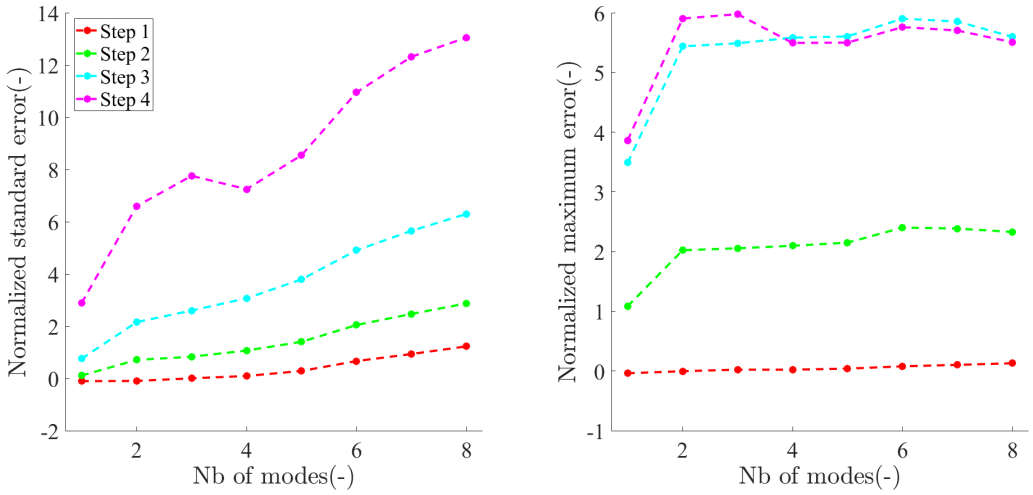

(a) (b)

Figure 9: Normalized standard deviation (a) and maximum (b) displacement errors as functions of the number of modes

For step 1, where the specimen state is the same as at the initial step, the damage indicators are really close to those obtained at the initial step. This observation confirms the ability of the method to apply when the specimen is not damaged.

3.2.3 Displacement error fields

In order to ensure that the projection error is localized near the crack tip, the corresponding fields are displayed in Figure 10. As the crack propagates, the displacement error around its tip increases. In addition, a residual displacement is observed due to the presence of the crack.

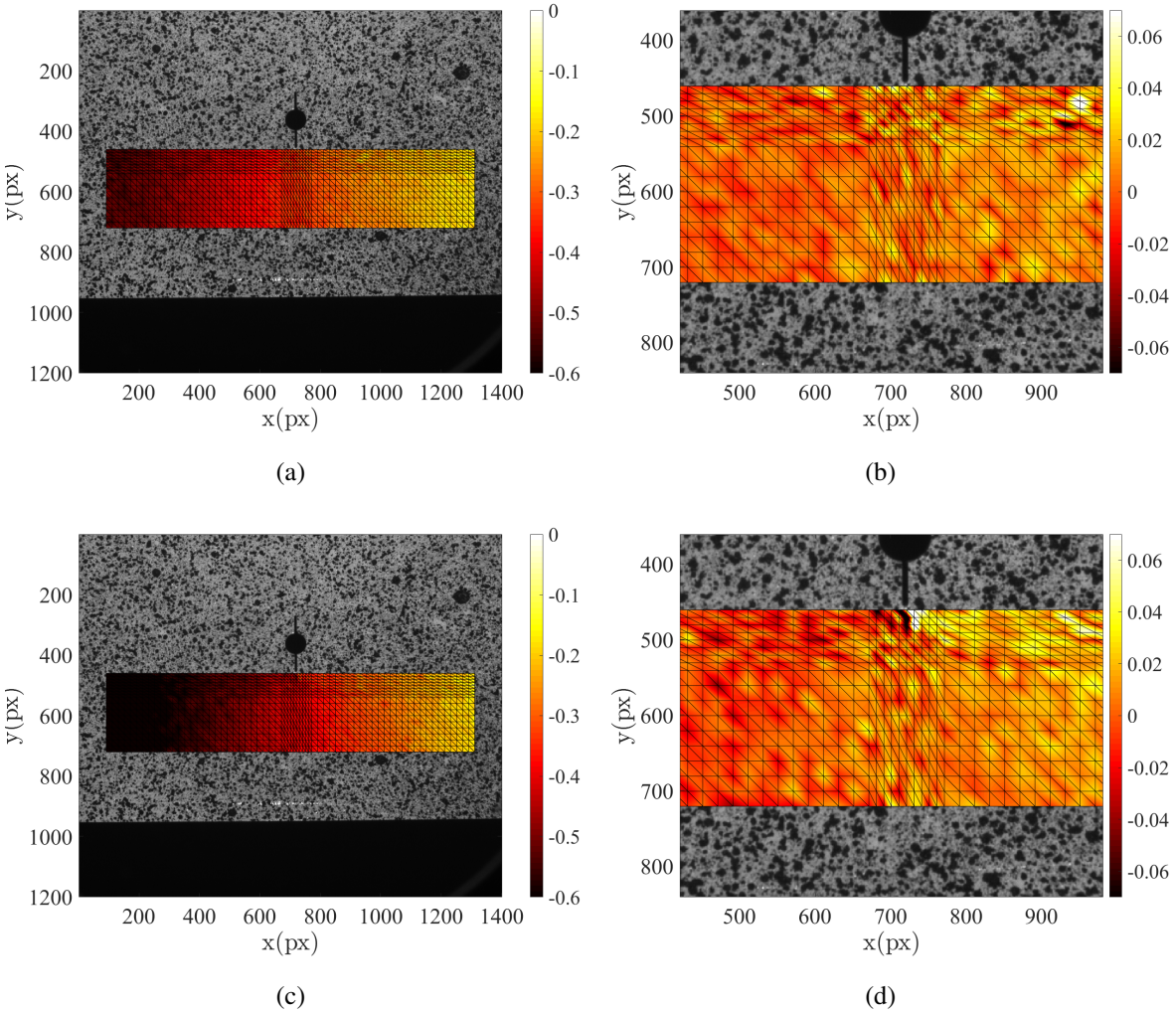

Figure 10: Displacements fields (expressed in px) along the x-direction for steps 1 (a) and 3 (c), and corresponding projection errors (b,d)

This phenomenon results in repetitive location of the error maximum (Figure 11). The two nodes where the maximum errors occurred at step 3 are in the vicinity of the crack tip.

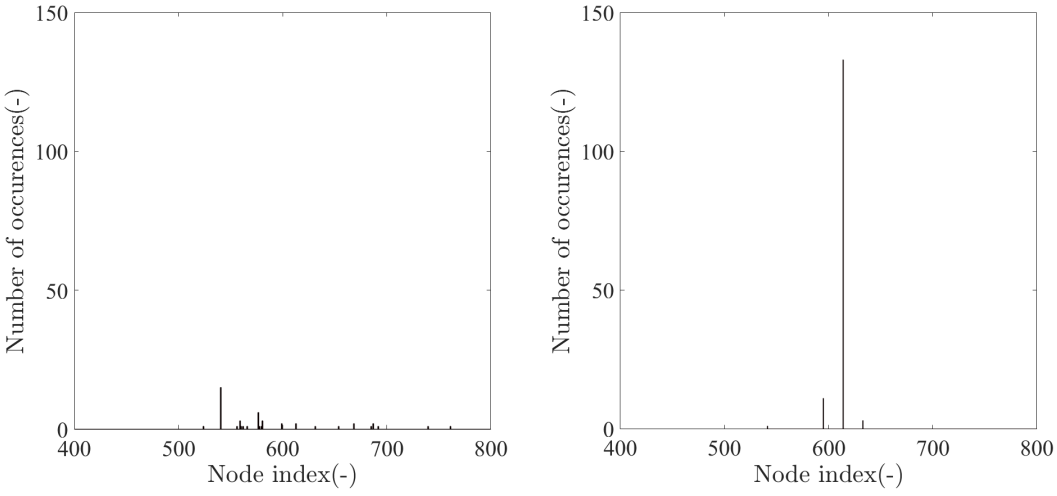

Figure 11: Locations of maximum error for the steps 1 (a) and 3 (b)

3.2.4 DIC residuals

An additional information is available thanks to DIC residuals. When DIC computations are performed and the solution is close to the actual displacement field, the residuals reduce to intrinsic camera noise. This is true under the condition that brightness conservation (1) be fulfilled. To be satisfied, no illumination variations should occur. Otherwise, brightness and contrast (BC) corrections should be performed. If the displacement field is not rich enough to completely account for gray level variations, its root mean square (RMS) will be higher. It may be due to mesh coarseness with regard to the displacement complexity, or discontinuity in the displacement field.

The experiment studied herein lasted 5 hours. Major illumination variations were prevented using artificial lighting but smaller ones unavoidably occurred. Brightness and contrast corrections were applied after the DIC computation was performed. They were performed with one Q8 element over the whole ROI. The RMS residuals before and after BC correction are plotted in Figure 12. The correction has little impact on the levels (*i*.e., about few gray levels for a 16-bit dynamic range), which confirms the very small illumination variations. Along the experimental steps, the RMS residual increases even after BC corrections. This means that the measured displacement field does not fully describe the actual kinematics of the test (*i*.e., the presence of the crack). The refinement with linear T3 elements in this area is not sufficient for fully describing the local complexity of the displacement field. Thus an increase in the residual norm is also an indicator of damage.

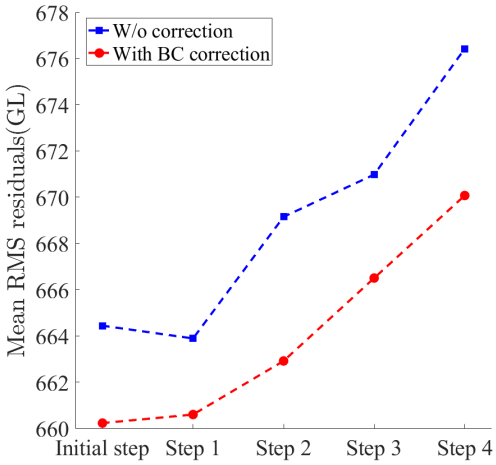

Figure 12: Comparison of mean RMS residuals before and after BC corrections for the five steps

Figure 13 confirms that the increase of residuals is located where the crack initiated, thus due to damage.

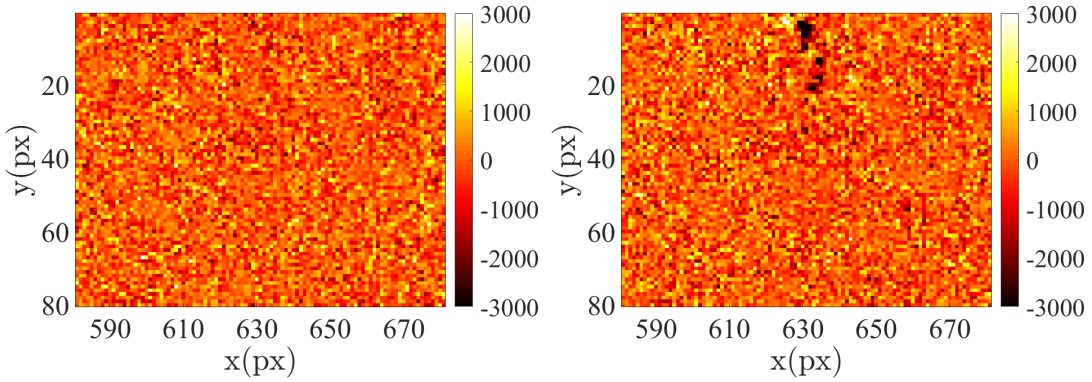

(a) (b)

Figure 13: Zoom around the crack tip of gray level residual maps at steps 1 (a) and 3 (b) when 16-bit images were registered

The DIC residual fields were also computed after displacement projection onto the modal basis. The mean and standard deviation of the displacement error indicators decreased as the selected number of modes increased. This is not the case for the RMS residuals. The RMS level is bounded by intrinsic camera noise and by interpolation errors. To evaluate the impact of the projection onto the modal basis, the residual difference before projection and after projection was calculated for the different steps of the experiment and is plotted in Figure 14. It is observed that damage influenced more the residuals after projection. The higher the damage

level, the higher the projection error. For step 2, the influence is really small, the difference with the values obtained at the initial step are largely due to interpolation errors. For step 4, the error due to modal projection is equivalent to that due to interpolation error. Thus, it is concluded that residuals are also a damage indicator, and displacement modal projection highlights it.

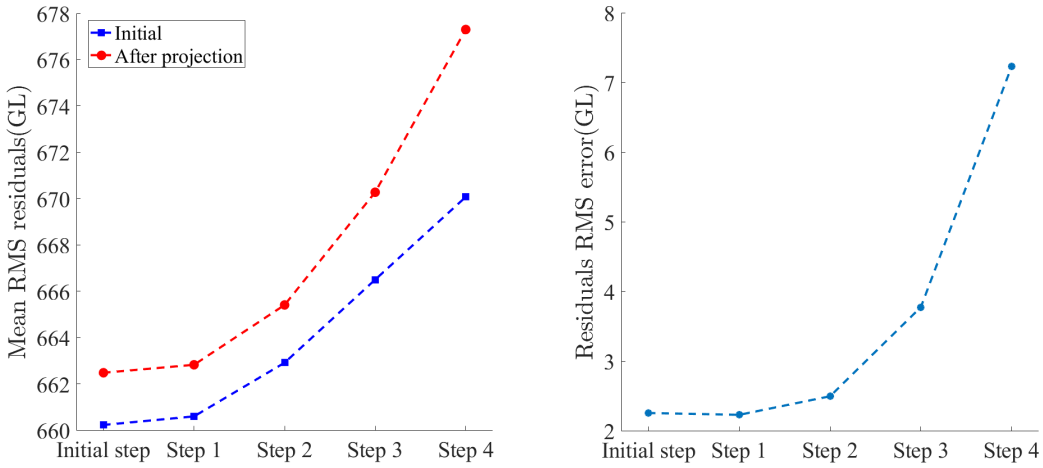

(a) (b)

Figure 14: (a) Comparison of RMS residuals with direct DIC and after projection onto the modal basis. (b) Error induced by projection onto the modal displacement basis

4 New DIC approach based on optimal extractors

In the following, the concept of optimal extractors and "one-step" DIC will be presented.

4.1 Optimal extractors

Integrated DIC consists in using as kinematic basis a space generated by a reduced set of fields motivated by the problem of interest [32]. For instance, the displacement field of Euler-Bernoulli beams subjected to flexural loading is measured with only six degrees of freedom per beam [58]. This technique reduces the number of unknowns in the DIC problem, and thus the associated measurement uncertainties. In the first (*i*.e., learning) phase, an appropriate displacement (modal) basis has to be set. This modal basis could be used directly as generalized shape functions. Thus, it is noted that the same reference image and kinematic basis can be used repeatedly. Hence it is worth precomputing all these repetitive aspects with what is called optimal *extractors* to accelerate the calculations. The underlying principle is presented in the sequel.

For each spatial mode $\boldsymbol{\Psi}_i$, which was determined in the learning phase, it is possible to determine its sensitivity field s_i

$$s_i(\boldsymbol{x}) = \boldsymbol{\Psi}_i(\boldsymbol{x}) \cdot \boldsymbol{\nabla} \hat{f}(\boldsymbol{x}) \tag{15}$$

Introducing matrix $[\boldsymbol{N}]$

$$N_{ij} = \sum_{\boldsymbol{x}} s_i(\boldsymbol{x}) s_j(\boldsymbol{x}) \tag{16}$$

it is possible to define an extractor field $\zeta_i(\boldsymbol{x})$, for each mode i, such that

$$\zeta_i(\boldsymbol{x}) = \sum_{j} N_{ij}^{-1} s_j(\boldsymbol{x}) \tag{17}$$

where N_{ij}^{-1} is the ij component of the inverse of matrix $[\boldsymbol{N}]$.

The amplitude $\chi_i(t)$ associated with the modal field $\boldsymbol{\Psi}_i(\boldsymbol{x})$ is determined by the scalar product of the extractor field with the field $\rho(\boldsymbol{x}, t) = g(\boldsymbol{x}, t) - f(\boldsymbol{x})$, which is again the difference in gray levels between the deformed image g and the reference image f

$$\chi_i(t) = \sum_{\boldsymbol{x}} \zeta_i(\boldsymbol{x}) \rho(\boldsymbol{x}, t) \tag{18}$$

The correlation residual η is calculated as the difference between the initial residual ρ and the gray level variations induced by modal displacement updates

$$\eta(\boldsymbol{x}, t) = \rho(\boldsymbol{x}, t) - \sum_{i} \chi_i(t) s_i(\boldsymbol{x}) \tag{19}$$

Thus, the main interest lies in the fact that for any number of deformed images, the extractors are computed once for all. One new image only requires a subtraction and a scalar product. These simple operations can be processed very fast (*e*.g., using GPU).

4.2 "One-step" DIC

From the learning stage, the statistics about the displacement amplitudes is also available. With such information, the goal is to further speed up DIC analyses yielding a good solution in one single step. DIC deals with nonlinear minimizations, based on iterative schemes [22, 23]. For each iteration, the summand of the cost function is linearized to compute incremental corrections to the sought degrees of freedom. This operation can be rephrased as computing the variation of local gray levels of the image is equal to the scalar product of the displacement by the gradient of the image. When the displacement is too large, the linear gray level variation approximation with the displacement is no longer valid, which implies that several iterations are necessary to converge to a satisfactory result.

One way to reach the right solution in a unique iteration is to perform appropriate image filtering. The filtering of an image consists in erasing details below a certain λ scale, often considered as constant over the whole ROI. This filtering operation is performed by convolving the initial image with a kernel (*e*.g., Gaussian), which tends toward zero for a distance to the origin greater than λ. The information is spread over an area covered by the filtering length. The gradient variations of the filtered image are thus attenuated. Such type of approach

was already used in multiscale DIC [55]. DIC computations were iteratively performed with progressively unblurred images. It enables for rapid convergence toward coarse solutions. Consequently, the following computations are initialized with previous displacement fields and then global convergence is faster as more details are restored in the image and in the displacement field.

Filtering is a way to restore DIC linearity. Estimating the correct displacement field in one single iteration is accessible provided appropriate image filters are used. The needed filtering is directly related to the displacement amplitude. When displacement amplitudes are small (*i*.e., less than 1 px), it is assumed that homogeneous filtering is sufficient due to small gray level variations. A simple test case to validate this assumption consists in calculating the best optimal filtering length to estimate rigid body translations with "one-step" DIC. A smooth Gaussian kernel was used, from the `matlab` function `imgaussfilt` [59]. In 2D, an isotropic Gaussian filter G reads

$$G(x,y) = \frac{1}{2\pi\lambda^2} \exp\left(-\frac{x^2+y^2}{2\lambda^2}\right) \tag{20}$$

where x and y are the pixel coordinates, λ the "filtering length" as called in this work. The same image and ROI were selected as in the previous section. The "deformed" images were artificially created with bi-cubic gray level interpolation. For each translation amplitude, the optimal filtering length is the one that minimizes the displacement error. Figure 15 shows that for subpixel displacement amplitudes, the filtering length is independent of the applied amplitude.

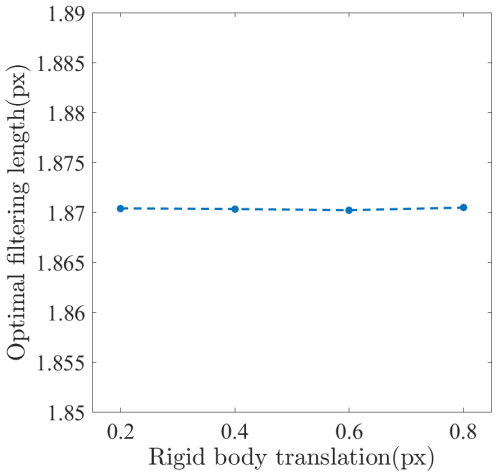

Figure 15: Optimal filtering length for subpixel rigid body translations

In the following, the application of one-step DIC is developed for sub-pixel displacements. In Appendix 7, a virtual application case is set for displacement amplitudes greater than 1 px. In particular, homogeneous filtering is no longer optimal, and another filtering strategy must be adopted.

5 Application of one-step DIC

In this section, first the calibration of the optimal filter length is carried out. Then, the application of "one-step" DIC is performed on the test case.

5.1 "One-step" DIC calibration

The method quality is evaluated by measuring the difference between the displacement measured via T3-DIC projected onto the modal basis and that obtained by "one-step" DIC. The objective is to find the optimal filter length that minimizes the displacement error over the whole set of pictures of the learning step. Several filtering lengths were tested ranging from 1 to 3 px. Three displacement modes were chosen. The results are plotted in Figure 16. It is found that the optimal filtering length is about 2.4 px. It is close to the previous (1.9) value found for rigid body translations. It is worth noting that the results presented in this subsection are only valid for the present test case. For any new sample, it is necessary to perform this step again. Moreover, the error fluctuation over the whole set of images tends to decrease with filter length increase. The error magnitude is correlated with the displacement amplitude. It is seen that excessive filtering with regard to local displacement magnitude may induce a loss of information. Being more accurate with high displacement amplitudes induces to be less accurate with lower amplitudes.

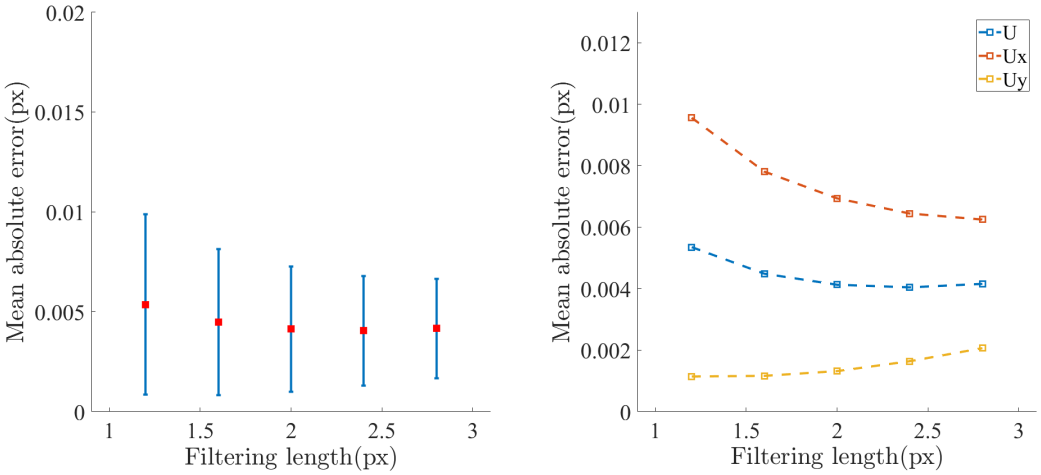

Figure 16: (a) Mean "One-step" DIC absolute error and its standard deviation over the whole set of images from the learning step. (b) Results detailed along each direction

Regarding the error along both directions, it is higher in the x-direction, along which the tensile load was applied. The error increases with filtering length along the y-direction. The overall absolute error is about 4×10^{-3} px, and 7×10^{-3} px in the x-direction. These levels are comparable with those of DIC uncertainties [22, 23]. Such observation validates the im-

plementation of this new technique. The fluctuations represented by the standard deviation are about 2×10^{-3} px for the displacement amplitude, and 5×10^{-3} px along the x-direction.

5.2 Example of extractor

The extractor defined in Equation (17) associated with the first mode and an original image optimally filtered are displayed in Figure 17. The extractor is directly linked to its corresponding mode shape. For example, for mode 1, the highest values of the extractor are on the left part where the displacement mode amplitudes are the highest.

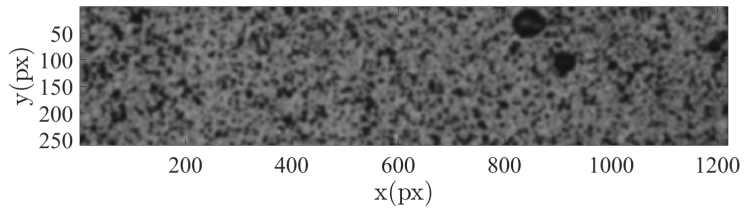

(a)

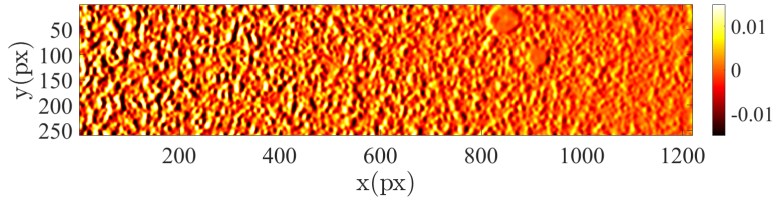

(b)

Figure 17: Filtered image (a) and extractor (b) for the first mode

5.3 "One-step" DIC application

The one-step DIC calculation was performed over the full sets of homogeneously filtered images. The filtering length was equal to 2.4 px as explained in the previous section. The mean values of RMS residuals are shown in Figure 18. The difference between the residual levels obtained in the initial step and the other steps are compared for both T-3 DIC and "one-step" DIC are also reported. First, the mean RMS level is approximately six times lower and its standard deviation is two times lower after filtering. It is due to local averaging of the information. However, the residual difference between the initial step and the others is nearly the same with T3-DIC and one-step DIC. Thus, by weighting the residual difference by their mean values, the jump induced by damage would be easier to spot.

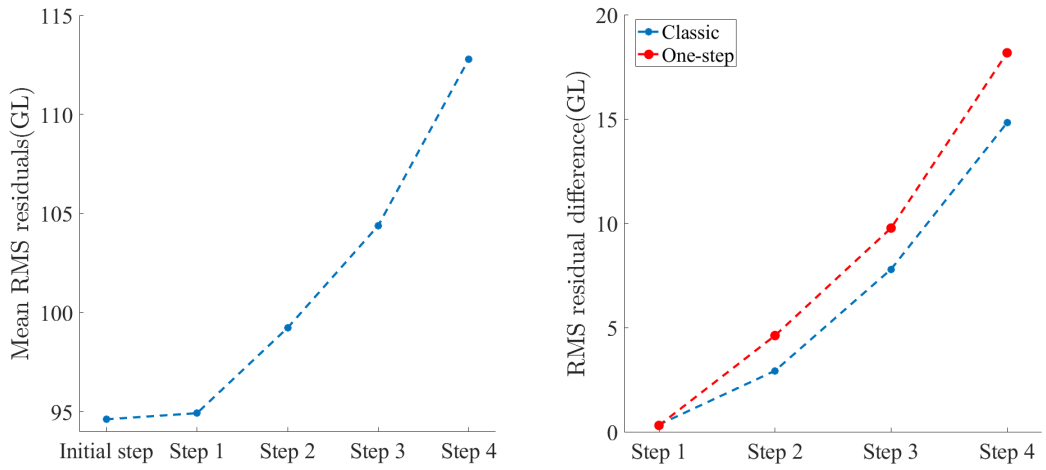

(a) (b)

Figure 18: Mean RMS residuals after one-step DIC (a). RMS residuals differences between the initial step and the other steps for both T3-DIC and "one-step" DIC (b)

6 Conclusion

In this work, a new method for structural health monitoring via DIC was proposed. This technique applies to structures that undergo the same loads repeatedly or statistically over time. Thus the deformations undergone by the surface of the structure depend on a limited number of parameters. All the measured displacement fields were condensed in a reduced kinematic basis. The method consisted of two steps:

- First, the kinematic basis was constructed. It corresponded to the learning stage. The selection criterion for the number of modes was based on the eigenvalues extracted from singular value decomposition of the measured spatiotemporal displacement field.
- Then, over time, the displacement fields measured by DIC were projected onto the kinematic basis. This part is the monitoring stage. Global error indicators made it possible to determine, over a large number of images, whether an error was present in the displacement field, and thus a defect that would be the source of this error.

The application case of this method also led to the establishment of the development of fast (*i*.e., "one-step") DIC. The idea is to perform DIC analyses in one single iteration. Starting from the calibration step of the kinematic basis, global modes and a map of maximum displacements were available. The use of an adapted filter allows the validity of the linear tangent operator of DIC to be extended. Hence, convergence is expected in a single iteration. This method was improved by pre-calculating image extractors based on kinematic modes. Then the error indicator coincided with the correlation residuals.

Perspectives about the presented algorithm and its validation are drawn. It may be interesting to use such SHM technique in more complex situations. For instance, multi-directional tests would be interesting to carry out because the modal basis would be of higher dimension. It may also be interesting to study the accuracy of one-step DIC on more complex deformations. In terms of error indicators, global values (standard deviation) and local estimates (maximum) for displacements were reported, but only global (RMS) values for the residuals. The ROI may be divided into squares or rectangles, and the RMS residuals may be evaluated over these smaller zones. Damage may be detectable earlier than with global indicators. Further, the algorithm must be coupled with a fixed imaging system that would acquire images continuously. For instance, in Ref. [60], arrays of 8 Mpx low cost cameras were used to capture images for DIC analyses of geotechnical specimen. This solution is economically feasible and may be applicable to large scale structures.

Acknowledgements

JC was supported by EdF R&D and ANRT through a CIFRE PhD grant. The help of Xavier Pinelli in the experiment reported herein is gratefully acknowledged.

7 Appendix: One step DIC with large displacements

In the previously presented work, the displacement amplitudes were less than 1 px. Thus a simple uniforms filtering was sufficient. In this appendix, the problem of using "one-step" DIC is addressed for larger amplitudes. More precisely, optimal inhomogeneous image filtering is proposed to better estimate displacement fields. It is assumed that the local filtering length λ is linked with the local displacement statistics. It can be the maximum, or the average weighted by a multiple of its standard deviation. In this case, it is related to the maximum recorded displacement, $\xi(\boldsymbol{x})$. The principle about this particular filtering is first described. Then, an artificial application case is set to illustrate the method.

7.1 Inhomogeneous filtering

This section describes inhomogenous filtering of an image. From a $\lambda(\boldsymbol{x})$ filter length field defined at each point of the ROI, N filter lengths $\widehat{\lambda}_i$, $i = 1, .., N$, are chosen to cover the range of λ values. The distribution of lengths can be equally distributed between the two extreme values, or follow a power law for instance.

For each of these lengths $\widehat{\lambda}_i$, a homogeneous filtering of image $f(\boldsymbol{x})$ denoted $\widetilde{f}_i(\boldsymbol{x})$ is carried out by convolution with a Gaussian kernel of standard deviation $\widehat{\lambda}_i$. These different filtering lengths will be used to create N homogeneously filtered images. It is proposed to approach image filtering at any scale λ by linear combination of images $\widehat{f}_i(\boldsymbol{x})$ and $\widehat{f}_{i+1}(\boldsymbol{x})$

$$\widehat{f}_\lambda(\boldsymbol{x}) \approx \alpha \widehat{f}_i(\boldsymbol{x}) + (1-\alpha)\widehat{f}_{i+1}(\boldsymbol{x}) \tag{21}$$

where α is a weighting coefficient to be determined. The minimization of the quadratic difference between the two members of this equation, on a small scale, provides the curvatures at the origin of the two convolution operators, Gaussian of standard deviation λ on the one hand, and weighted sum of the two filters of lengths $\widehat{\lambda}_i$ and $\widehat{\lambda}_{i+1}$. This observation leads to the weighting coefficient

$$\alpha = \frac{\widehat{\lambda}_{i+1}^2 - \lambda^2}{\widehat{\lambda}_{i+1}^2 - \widehat{\lambda}_i^2} \tag{22}$$

The advantage of this approximation is that it is performed in the real space. For each pixel position, it is easy to identify the weights $\alpha_i(\boldsymbol{x})$ to be assigned to the N filtered images, and to calculate the inhomogeneously filtered image by mere linear combination.

7.2 Filter calibration

In this part, the appropriate filtering coefficients are set depending on the locally encountered displacement. To achieve such goal, it is chosen to select the best homogeneous filtering length that minimizes displacement errors with artificial rigid body translations. Then, the function that associates the filtering length to the displacement amplitude is set. The same specimen and ROI as previously considered were selected. The results are plotted in Figure 19. First, it is observed that for translation amplitudes less than 1 px, the filtering length is independent of the translation amplitude. Above 1 px, the ratio between the optimal filtering length and the translation amplitude is about 4. No explanation is proposed to explain this sudden gap.

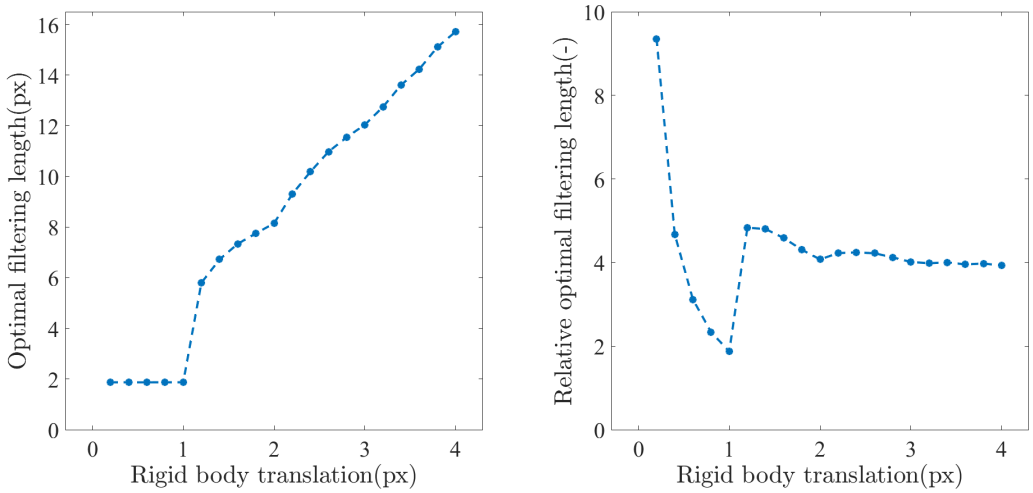

(a) (b)

Figure 19: Absolute (a) and relative (b) optimal filtering lengths

7.3 Application to heterogeneous displacement fields

In this subsection, the interest of inhomogeneous filtering is shown when large displacement amplitudes (*i*.e., greater than 1 px) are encountered. Displacement fields related to tensile tests

were tested:

- One relative to uniform strain over the whole ROI. It is referred to as Case 1 in the following.
- One related to the first displacement mode found in Section 2.3. It is referred to as Case 2.

The performance of the filtering strategy is tested for maximum amplitudes ranging from 0.4 to 4 px, by steps of 0.4 px. The displacement map used as reference for filtering is based on a maximum amplitude of 4 px. Inhomogeneous filtering is carried out based on the results observed in Section 7.2. Depending on the local maximum amplitude, different filtering lengths are selected. For pixels where the maximum encountered displacement is less than one pixel, the filtering length is equal to 1.9 px. For pixels where the maximum amplitude is greater than 1 px, the filtering length is equal to 4 times the displacement amplitude. As explained above, an approximation based on few homogeneously filtered images is performed. Four filtering lengths are chosen, namely, 1.9, 4, 8, 12 and 16 px. This choice is arbitrary.

The reference displacement map and the corresponding filtered image are displayed for Case 1 in Figure 20. The effect of inhomogeneous filtering is visible between the right part (*i*.e., small displacement amplitudes) and the left part (*i*.e., higher displacement levels).

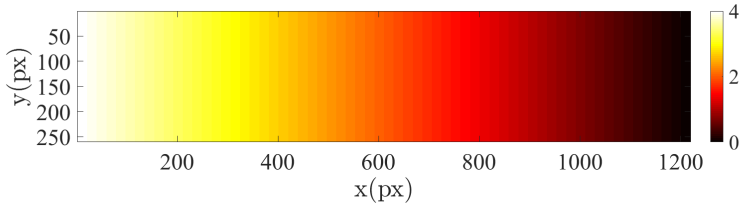

(a)

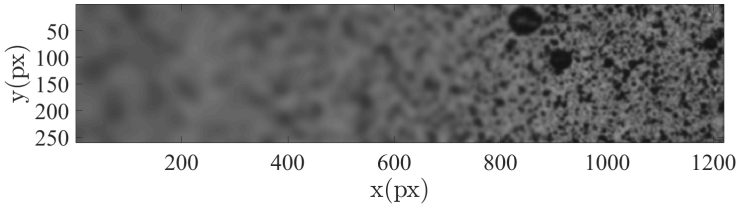

(b)

Figure 20: (a) Displacement map along x-direction in pixels. (b) Corresponding adaptively filtered image

There are two ways to evaluate the performance of the approach. First, one may look at the one-step DIC error over the whole range of displacement amplitudes. The RMS of the error

vector is thus a good indicator. Second, the prediction error is studied for the largest magnitude. The comparison between homogeneous and inhomogeneous filterings for both indicators are plotted in Figures 21 and 22 for Cases 1 and 2, respectively.

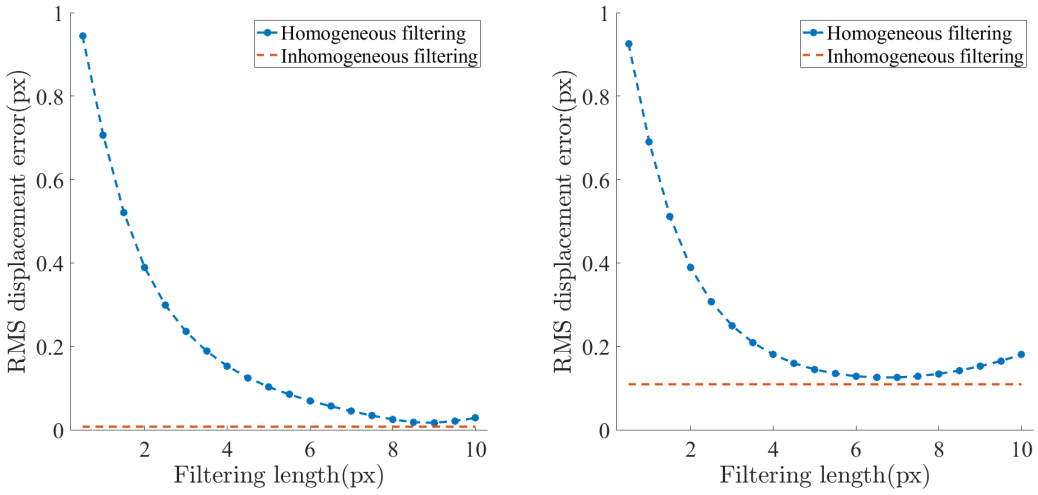

(a) (b)

Figure 21: One-step DIC error with homogeneous and inhomogeneous filtering over the whole set of displacement fields, for Cases 1 (a) and 2 (b)

The results are improved with inhomogeneous filtering for both indicators and both cases, for any filter length. This innovative way of filtering is more adapted. This new technique yields lower displacement errors, when large amplitudes of displacements occur. Moreover, with a generic calibration, the results are relevant for two different artificial cases, while the best respective homogeneous filtering lengths differ.

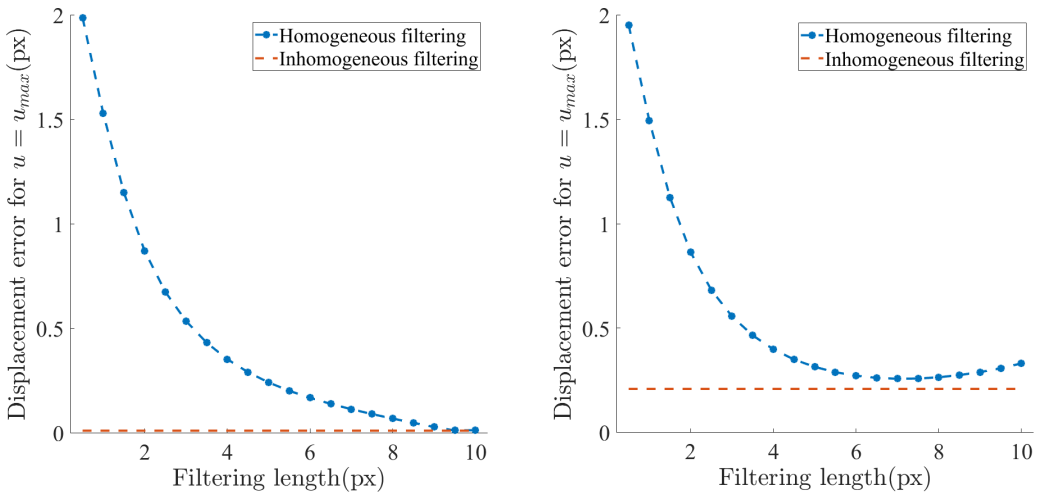

Figure 22: One-step DIC error with homogeneous and inhomogeneous filtering for the larger displacement magnitude, for Cases 1 (a) and 2 (b)

References

[1] ST Rolfe and JM Barsom. Fracture and fatigue control in structures: Applications of fracture mechanics. ASTM International, 1977.

[2] CR Farrar and K Worden. An introduction to structural health monitoring. Philosophical Transactions of the Royal Society A: Mathematical, Physical and Engineering Sciences, 365(1851):303–315, 2007.

[3] A Rytter. Vibrational based inspection of civil engineering structures. PhD thesis, Dept. of Building Technology and Structural Engineering, Aalborg University, 1993.

[4] M Benedetti, V Fontanari, and D Zonta. Structural health monitoring of wind towers: remote damage detection using strain sensors. Smart Materials and Structures, 20(5):055009, 2011.

[5] H Bang, S Ko, M Jang, and H Kim. Shape estimation and health monitoring of wind turbine tower using a fbg sensor array. In 2012 IEEE International Instrumentation and Measurement Technology Conference Proceedings, pages 496–500. IEEE, 2012.

[6] MA Coulthard. Image processing for automatic surface defect detection. In Third International Conference on Image Processing and its Applications, 1989., pages 192–196. IET, 1989.

[7] H Jia, YL Murphey, J Shi, and T Chang. An intelligent real-time vision system for surface defect detection. In Proceedings of the 17th International Conference on Pattern Recognition, 2004. ICPR 2004., volume 3, pages 239–242. IEEE, 2004.

[8] SH Bhandari and SM Deshpande. A simple approach to surface defect detection. 2008 IEEE Region, 10:8–10, 2008.

[9] E Hildreth and D Marr. Theory of edge detection. Proceedings of Royal Society of London, 207(187-217):9, 1980.

[10] J Canny. A computational approach to edge detection. IEEE Transactions on pattern analysis and machine intelligence, 8:679–698, 1986.

[11] F Bouchara, M Bertrand, S Ramdani, and M Haydar. Sub-pixel edge fitting using b-spline. In International Conference on Computer Vision/Computer Graphics Collaboration Techniques and Applications, pages 353–364. Springer, 2007.

[12] T Hermosilla, E Bermejo, A Balaguer, and LA Ruiz. Non-linear fourth-order image interpolation for subpixel edge detection and localization. Image and vision computing, 26(9):1240–1248, 2008.

[13] M Hagara and P Kulla. Edge detection with sub-pixel accuracy based on approximation of edge with erf function. Radioengineering, 20(2):516–524, 2011.

[14] P Dare, H Hanley, C Fraser, B Riedel, and W Niemeier. An operational application of automatic feature extraction: the measurement of cracks in concrete structures. The Photogrammetric Record, 17(99):453–464, 2002.

[15] T Yamaguchi and S Hashimoto. Fast crack detection method for large-size concrete surface images using percolation-based image processing. Machine Vision and Applications, 21(5):797–809, 2010.

[16] I Abdel-Qader, O Abudayyeh, and ME Kelly. Analysis of edge-detection techniques for crack identification in bridges. Journal of Computing in Civil Engineering, 17(4):255–263, 2003.

[17] X Li, C Gao, Y Guo, F He, and Y Shao. Cable surface damage detection in cable-stayed bridges using optical techniques and image mosaicking. Optics & Laser Technology, 110:36–43, 2019.

[18] YS Mohamed, HM Shehata, M Abdellatif, and TH Awad. Steel crack depth estimation based on 2d images using artificial neural networks. Alexandria Engineering Journal, 2019.

[19] CV Dung. Autonomous concrete crack detection using deep fully convolutional neural network. Automation in Construction, 99:52–58, 2019.

[20] CV Dung, H Sekiya, S Hirano, T Okatani, and C Miki. A vision-based method for crack detection in gusset plate welded joints of steel bridges using deep convolutional neural networks. Automation in Construction, 102:217–229, 2019.

[21] M Alipour and DK Harris. Increasing the robustness of material-specific deep learning models for crack detection across different materials. Engineering Structures, 206:110157, 2020.

[22] MA Sutton, JJ Orteu, and H Schreier. Image correlation for shape, motion and deformation measurements: Basic Concepts, Theory and Applications. Springer, New York, NY (USA), 2009.

[23] F Hild and S Roux. Digital image correlation. In P Rastogi and E Hack, editors, Optical Methods for Solid Mechanics. A Full-Field Approach, pages 183–228, Weinheim (Germany), 2012. Wiley-VCH.

[24] MA Sutton. Computer vision-based, noncontacting deformation measurements in mechanics: a generational transformation. Applied Mechanics Reviews, 65(5):050802, 2013.

[25] JN Périé, S Calloch, C Cluzel, and F Hild. Analysis of a multiaxial test on a c/c composite by using digital image correlation and a damage model. Experimental Mechanics, 42(3):318–328, 2002.

[26] A El Bartali, V Aubin, and S Degallaix. Fatigue damage analysis in a duplex stainless steel by digital image correlation technique. Fatigue & Fracture of Engineering Materials & Structures, 31(2):137–151, 2008.

[27] R Munier, C Doudard, S Calloch, and B Weber. Digital image correlation and infrared measurements to determine the influence of a uniaxial pre-strain on fatigue properties of a dual phase steel. In EPJ Web of Conferences, volume 6, page 37007. EDP Sciences, 2010.

[28] C Roux-Langlois, A Gravouil, M-C Baietto, J Réthoré, F Mathieu, F Hild, and S Roux. Dic identification and x-fem simulation of fatigue crack growth based on the williams' series. International Journal of Solids and Structures, 53:38–47, 2015.

[29] M Bolhassani, S Rajaram, AA Hamid, A Kontsos, and I Bartoli. Damage detection of concrete masonry structures by enhancing deformation measurement using dic. In Nondestructive Characterization and Monitoring of Advanced Materials, Aerospace, and Civil Infrastructure 2016, volume 9804, page 980411. International Society for Optics and Photonics, 2016.

[30] S Nag-Chowdhury, H Bellégou, I Pillin, M Castro, P Longrais, and JF Feller. Crossed investigation of damage in composites with embedded quantum resistive strain sensors (sqrs), acoustic emission (ae) and digital image correlation (dic). Composites Science and Technology, 160:79–85, 2018.

[31] R Wu, D Zhang, Q Yu, Y Jiang, and D Arola. Health monitoring of wind turbine blades in operation using three-dimensional digital image correlation. Mechanical Systems and Signal Processing, 130:470–483, 2019.

[32] S Roux and F Hild. Stress intensity factor measurements from digital image correlation: post-processing and integrated approaches. International journal of fracture, 140(1-4):141–157, 2006.

[33] JR Yates, M Zanganeh, and YH Tai. Quantifying crack tip displacement fields with dic. Engineering Fracture Mechanics, 77(11):2063–2076, 2010.

[34] S McNeill, W Peters, and MA Sutton. Estimation of stress intensity factor by digital image correlation. Engineering fracture mechanics, 28(1):101–112, 1987.

[35] J Rethore, A Gravouil, F Morestin, and A Combescure. Estimation of mixed-mode stress intensity factors using digital image correlation and an interaction integral. International Journal of Fracture, 132(1):65–79, 2005.

[36] R Hamam, F Hild, and S Roux. Stress intensity factor gauging by digital image correlation: Application in cyclic fatigue. Strain, 43(3):181–192, 2007.

[37] F Mathieu, F Hild, and S Roux. Identification of a crack propagation law by digital image correlation. International Journal of Fatigue, 36(1):146–154, 2012.

[38] AF Cinar, SM Barhli, D Hollis, M Flansbjer, RA Tomlinson, TJ Marrow, and M Mostafavi. An autonomous surface discontinuity detection and quantification method by digital image correlation and phase congruency. Optics and Lasers in Engineering, 96:94–106, 2017.

[39] J Rupil, S Roux, F Hild, and L Vincent. Fatigue microcrack detection with digital image correlation. The Journal of Strain Analysis for Engineering Design, 46(6):492–509, 2011.

[40] B Zhao, D Lei, J Fu, L Yang, and W Xu. Experimental study on micro-damage identification in reinforced concrete beam with wavelet packet and dic method. Construction and Building Materials, 210:338–346, 2019.

[41] N Eleftheroglou, D Zarouchas, T Loutas, R Alderliesten, and R Benedictus. Structural health monitoring data fusion for in-situ life prognosis of composite structures. Reliability Engineering & System Safety, 178:40–54, 2018.

[42] C Jailin. Full field modal measurement with a single standard camera. Optics and Lasers in Engineering, 107:265–272, 2018.

[43] Y Wang. Fatigue Thermique à grand nombre de cycles d'un acier inoxydable austénitique: apport des mesures de champs pour l'identification du chargement et le suivi in-situ de l'endommagement. PhD thesis, Université Paris-Saclay, 2019.

[44] J-C Passieux, R Bouclier, and J-N Périé. A space-time pgd-dic algorithm. Experimental Mechanics, 58(7):1195–1206, 2018.

[45] TC Chu, WF Ranson, and Michael A Sutton. Applications of digital-image-correlation techniques to experimental mechanics. Experimental mechanics, 25(3):232–244, 1985.

[46] B Pan. Recent progress in digital image correlation. Experimental mechanics, 51(7):1223–1235, 2011.

[47] B Peng, Q Zhang, W Zhou, X Hao, and L Ding. Modified correlation criterion for digital image correlation considering the effect of lighting variations in deformation measurements. Optical Engineering, 51(1):017004, 2012.

[48] W Tong. An evaluation of digital image correlation criteria for strain mapping applications. Strain, 41(4):167–175, 2005.

[49] AD Kammers and S Daly. Digital image correlation under scanning electron microscopy: methodology and validation. Experimental Mechanics, 53(9):1743–1761, 2013.

[50] VF Sciuti, RB Canto, J Neggers, and F Hild. On the benefits of correcting brightness and contrast in global digital image correlation: Monitoring cracks during curing and drying of a refractory castable. Optics and Lasers in Engineering, 136:106316, 2020.

[51] A Mendoza, J Schneider, E Parra, E O, and S Roux. Differentiating 3d textile composites: A novel field of application for digital volume correlation. Composite Structures, 208:735–743, 2019.

[52] IT Joliffe and BJT Morgan. Principal component analysis and exploratory factor analysis. Statistical methods in medical research, 1(1):69–95, 1992.

[53] A Chatterjee. An introduction to the proper orthogonal decomposition. Current science, pages 808–817, 2000.

[54] J Neggers, O Allix, F Hild, and S Roux. Big data in experimental mechanics and model order reduction: today's challenges and tomorrow's opportunities. Archives of Computational Methods in Engineering, 25(1):143–164, 2018.

[55] F Hild, B Raka, M Baudequin, S Roux, and F Cantelaube. Multiscale displacement field measurements of compressed mineral-wool samples by digital image correlation. Applied Optics, 41:6815–6828, 2002.

[56] J Gamot, T Lasserre, L Richard, J Neggers, N Swiergiel, and F Hild. Calibrating thermoelastic stress analysis with integrated digital image correlation: Application to fatigue cracks. The Journal of Strain Analysis for Engineering Design, 54(5-6):320–330, 2019.

[57] H Leclerc, J Neggers, F Mathieu, S Roux, and F Hild. Correli 3.0. Agence pour la Protection des Programmes, Paris, IDDN.FR.001.520008.000.S.P.2015.000.31500, 2015.

[58] F Hild, S Roux, N Gras, Rand Guerrero, M E Marante, and J Flórez-López. Displacement measurement technique for beam kinematics. Optics and Lasers in Engineering, 47(3-4):495–503, 2009.

[59] The Mathworks, Inc., Natick, Massachusetts. MATLAB version 9.3.0.713579 (R2017b), 2017.

[60] GN Eichhorn, A Bowman, SK Haigh, and S Stanier. Low-cost digital image correlation and strain measurement for geotechnical applications. Strain, 56(6):e12348, 2020.